THE JOURNAL OF PHYSICAL CHEMISTRY LETTERS
A JOURNAL OF THE AMERICAN CHEMICAL SOCIETY

pubs.acs.org/JPCL Letter

Revealing the Pressure-Induced Phase Transformation of Xenotime $TbPO_4$ via *In Situ* Photoluminescence Spectroscopy

Jai Sharma, Brandon Reynolds, Matthew J. Crane, and Corinne E. Packard*

Cite This: *J. Phys. Chem. Lett.* 2024, 15, 4294−4300 Read Online

ACCESS | Metrics & More | Article Recommendations | Supporting Information

ABSTRACT: The pressure-induced phase transformations of certain rare earth (RE) orthophosphates have attracted broad interest from geoscience to structural ceramics. Studying these transformations has required *in situ* Raman spectroscopy or synchrotron X-ray diffraction (XRD), each of which suffers from poor signal or limited accessibility, respectively. This study exploits the photoluminescence (PL) of Tb^{3+} ions and the unique sensitivity of PL to the local bonding environment to interrogate the symmetry-reducing xenotime−monazite phase transformation of $TbPO_4$. At pressures consistent with the XRD-based phase transformation onset pressure of 8.7(6) GPa, PL spectra show new peaks emerging as well as trend changes in the centroids and intensity ratios of certain PL bands. Furthermore, PL spectra of recovered samples show transformation is irreversible. Hysteresis in certain PL band intensity ratios also reveals the stress history in $TbPO_4$. This *in situ* PL approach can be applied to probe pressure-induced transformations and crystal field distortions in other RE-based oxide compounds.

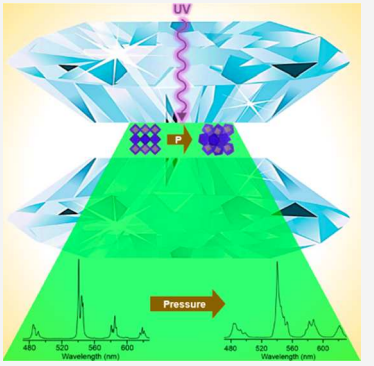

Rare earth orthophosphates ($REPO_4$s) make up a highly refractory class of ceramics with multidisciplinary appeal.[1] These materials naturally occur in xenotime and monazite minerals, whose properties and formation are of great interest in geoscience and in mining.[2−5] $REPO_4$s have also been synthesized with high purity and precise RE doping for optical applications (e.g., phosphors, lasers, and scintillators).[6−10] In recent decades, $REPO_4$s have been investigated as potential fiber coatings in oxide−oxide ceramic matrix composites (CMCs) for aerospace components subject to extreme conditions.[11,12] In particular, $REPO_4$ compositions that undergo pressure-induced phase transformations offer the possibility of additional toughening and plasticity mechanisms in CMCs.[13,14] Phase transformation may also be relevant to tuning the photoluminescent properties of $REPO_4$s or other RE-based materials for fundamental, low-symmetry RE studies as well applications in sensing, laser cooling, and photonic devices.[15−21]

Exploiting the pressure-induced phase transformation of $REPO_4$s begins with an understanding of their polymorphism. In equilibrium at 1 atm, the $REPO_4$ crystal structure is largely determined by the ionic radius. Compositions with smaller RE^{3+} ionic radii (RE = Tb^{3+}−Lu^{3+}, Sc^{3+}, and Y^{3+}) crystallize in the xenotime structure (tetragonal, $I4_1/amd$), while those with larger RE^{3+} ionic radii (RE = La^{3+}−Gd^{3+}) crystallize in the monazite structure (monoclinic, $P2_1/n$) as shown in Figure 1.[22] At high pressure (HP), certain xenotime compositions (RE = Tb^{3+}−Tm^{3+} and Y^{3+}) transform into the monazite structure.[23−25] This transformation involves an increase in RE−O coordination (8 → 9), the loss of RE site symmetry (D_{2d} → C_1), and a volume loss of ∼5%. The transformation occurs via the reconfiguration of RE−O bonds, while the PO_4 tetrahedra remain effectively rigid.[26]

Finding the onset pressure (P_{onset}) of the xenotime−monazite phase transformation in $REPO_4$s typically requires *in situ* diamond anvil cell (DAC) Raman spectroscopy (RS) or synchrotron X-ray diffraction (XRD). For the composition of interest in this study, $TbPO_4$, RS-based P_{onset} values of ∼9.5 and 10.1 GPa have been reported by Tatsi et al.[29] and Musselman et al.,[30] respectively. Both studies report some degree of phase transformation irreversibility and utilize pressure-transmitting media that are hydrostatic at P_{onset} (e.g., 4:1 methanol/ethanol and 16:3:1 methanol/ethanol/water). Sharma et al. performed a $TbPO_4$ XRD experiment with neon pressure medium and report P_{onset} and transformation end pressure (P_{end}) values of 8.7(6) and 13.7(10) GPa, respectively.[31] Lopez-Solano et al.'s $TbPO_4$ XRD study (also using neon pressure medium) reports a higher P_{onset} of 9.9 GPa; however, this value appears to be an overestimation for reasons discussed in the XRD study by Sharma et al.[32]

Although both RS and synchrotron XRD can deliver unique material insight, they each have significant limitations. RS generally suffers from a low signal-to-noise ratio due to the low probability of Raman scattering, and this ratio only degrades

Received: January 19, 2024
Revised: April 8, 2024
Accepted: April 9, 2024
Published: April 15, 2024

https://doi.org/10.1021/acs.jpclett.4c00196
J. Phys. Chem. Lett. 2024, 15, 4294−4300

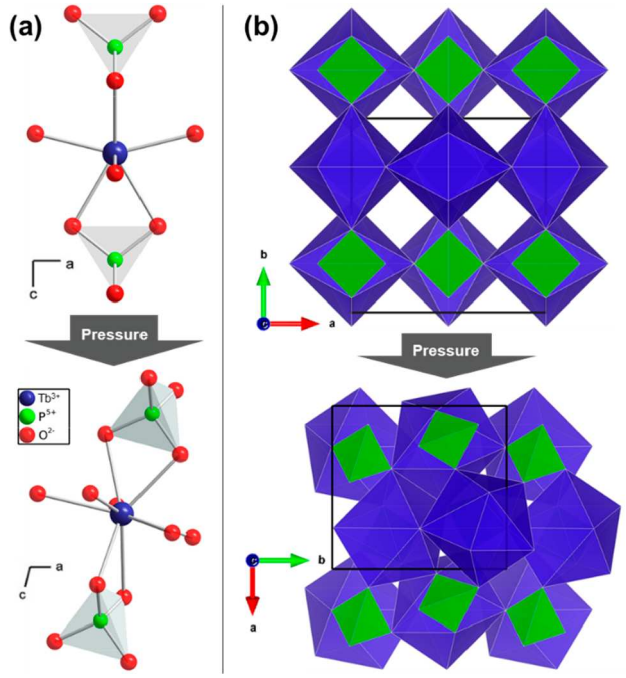

Figure 1. Structural changes in $TbPO_4$ during the pressure-induced xenotime−monazite phase transformation. (a) Tb^{3+} local bonding environment. Violet, green, and red spheres represent the Tb^{3+}, P^{5+}, and O^{2-} ions, respectively. Adapted from ref 27. Copyright 2019 Elsevier. (b) [001] views of the crystal structure. Violet polyhedra, green tetrahedra, and the black box represent the Tb−O cage, PO_4 groups, and the unit cell boundary, respectively. Crystal structures generated using VESTA.[28]

with pressure.[33−35] Moreover, the Raman-active phonon modes observed do not necessarily reflect the RE^{3+} local environment, which is what changes dramatically during the xenotime−monazite phase transformation. The RE^{3+} local environment can be probed using certain synchrotron X-ray techniques (e.g., single-crystal diffraction and inelastic scattering); however, synchrotron beamtime access is limited.

Given the well-known photoluminescent behavior of RE^{3+} ions, which are intrinsic to (or easily doped into) $REPO_4$s,[36,37] photoluminescence (PL) spectroscopy is a potentially promising technique for characterizing the xenotime−monazite transformation due to the high sensitivity of RE^{3+} PL to its symmetry and local site bonding environment.[38] Most PL of RE^{3+} ions stems from transitions between 4f configurational states, which are sensitive to changes in the local environment. Local environmental changes can cause differences in the number of peaks and transition strength in PL spectra.[39] In the case of xenotime $REPO_4$s, Lösch et al. discovered PL from Eu^{3+} dopants changed in the presence of non-xenotime $REPO_4$ phases in the host.[40] Lösch et al. attribute those PL changes to the impurity phases yielding different Eu^{3+} site symmetries. In addition, Yang et al. reported ambient-pressure PL emission spectra of $TbPO_4$ powder synthesized in the xenotime and metastable monazite phases, and the clearest difference between these spectra is the profile of the green emission band (~543 nm).[41] In monazite, this band has a broader and weaker low-energy shoulder and lacks the multiple local maxima seen in xenotime. More detailed analysis of this band is precluded by the limited spectral resolution. The sensitivity of RE^{3+} PL to the local environment has also been observed at HP by Runowski et al., who performed *in situ* DAC PL

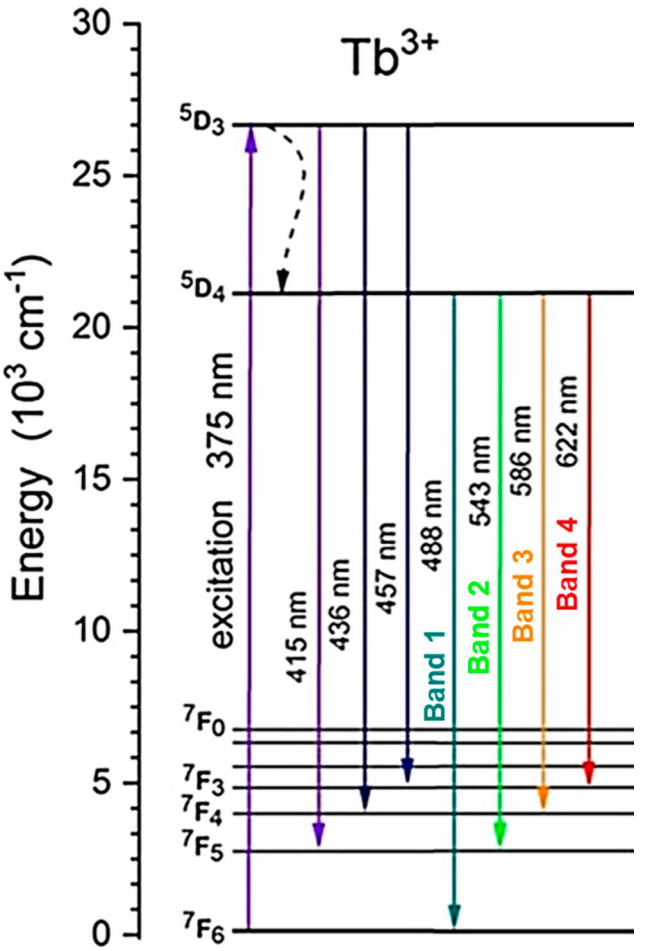

Figure 2. Dieke diagram showing the 4f intraconfigurational energy levels of Tb^{3+}. Excitation is shown with the upward arrow, and emissions are shown with downward arrows. The dashed and solid downward arrows represent phonon and photon emission, respectively. Adapted from ref 42. Copyright 2019 IOP Publishing.

spectroscopy on an up-converting composition, YPO_4 doped with Yb^{3+} and Tm^{3+}.[16] Runowski et al. noted PL band centroids and band intensity ratios (BIRs) exhibit continuous changes during loading and discontinuities at pressures consistent with the xenotime−monazite transformation of YPO_4. In addition to probing the RE^{3+} local environment, PL provides a signal stronger than that of RS and greater accessibility than synchrotron X-ray techniques.[35]

This *in situ* DAC PL spectroscopy study exploits the PL of intrinsic Tb^{3+} ions in $TbPO_4$ to detect the pressure-induced xenotime−monazite transformation. $TbPO_4$ is the $REPO_4$ chosen for this study, as it undergoes the pressure-induced xenotime−monazite transformation and has visible PL under ultraviolet (UV) excitation. Unlike the study by Runowski et al.,[16] this work involves direct excitation rather than up-conversion and requires no dopants to generate visible PL. Furthermore, the findings of this HP study are particularly valuable as the direct excitation PL of $TbPO_4$, or of any other xenotime $REPO_4$, has been reported only at ambient pressure.[41,43] Irreversible pressure-induced changes observed in PL spectra may also serve as indicators of stress history, which may be advantageous in potential CMC fiber coating applications.

https://doi.org/10.1021/acs.jpclett.4c00196
J. Phys. Chem. Lett. 2024, 15, 4294−4300

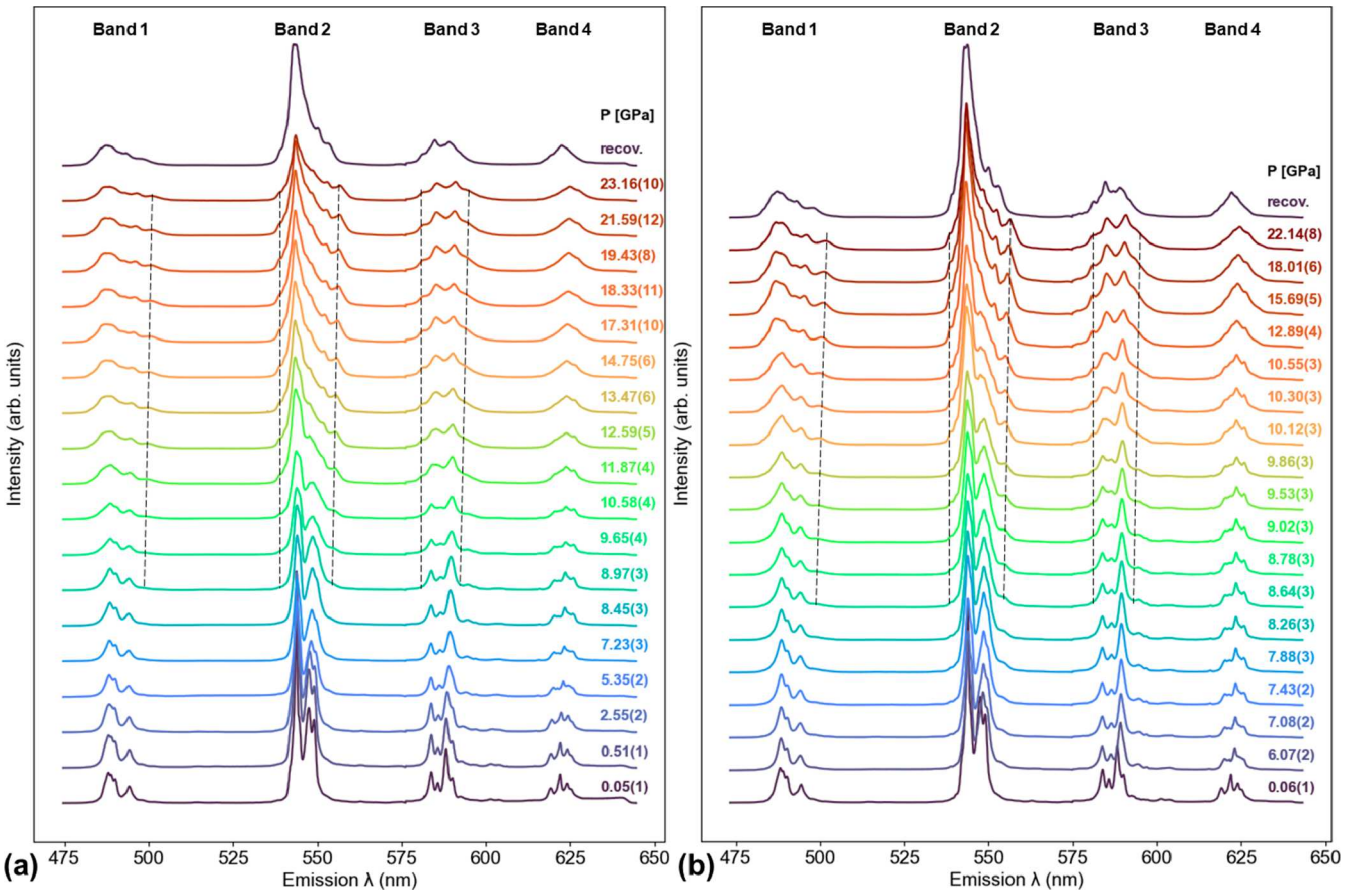

Figure 3. Pressure evolution of PL spectra from (a) experiment 1 and (b) experiment 2. Both experiments show pressures above P_{onset} as well as the spectrum of the recovered sample (at 1 atm). Numbers in parentheses after the pressure values represent the standard deviation in the last digit of the pressure. Dashed lines are visual guides for the peaks emerging at HP.

Each $TbPO_4$ PL spectrum contains four bands representing 4f intraconfigurational transitions of Tb^{3+} ($^5D_4 \rightarrow {}^7F_6$, $^5D_4 \rightarrow {}^7F_5$, $^5D_4 \rightarrow {}^7F_4$, and $^5D_4 \rightarrow {}^7F_3$) as shown in Figure 2.[44] Stark splitting ($\sim 10^2$ cm^{-1}) of the energy levels involved in these transitions is induced primarily by crystal field effects and causes each band to consist of multiple peaks.[39,45] For the sake of simplicity in the text, the PL bands generated by the $^5D_4 \rightarrow {}^7F_6$, $^5D_4 \rightarrow {}^7F_5$, $^5D_4 \rightarrow {}^7F_4$, and $^5D_4 \rightarrow {}^7F_3$ emissions are denoted as bands 1−4, respectively.

Five DAC experiments [named experiments 1−5 (Exp. 1−Exp. 5, respectively)] were conducted at room temperature, and they all involved a phase-pure xenotime $TbPO_4$ powder sample, a ruby pressure calibrant,[46] a 16:3:1 methanol/ethanol/water (MEW) pressure-transmitting medium, and 301 stainless steel gaskets. Exp. 4 and Exp. 5 are limited to pressures below the xenotime−monazite P_{onset}, while Exp. 1, Exp. 2, and Exp. 3 include P_{onset}. In addition, Exp. 3 and Exp. 4 do not include PL spectra of the recovered sample (upon returning to 1 atm), while Exp. 1, Exp. 2, and Exp. 5 do. In each experiment, a 375 nm pulsed laser (290 W/cm^2 average intensity) is used to excite the sample through a 10× objective lens via the $^7F_6 \rightarrow {}^5D_3$ transition. The emitted light from the sample is then focused and collected via a monochromator, where the PL spectra are recorded on a CCD (charge-coupled device) camera. Additional details about sample synthesis, phase purity verification, and experimental details, including the DAC configuration and PL measurements, are provided in the Supporting Information. In addition, the number in parentheses after a pressure value represents the standard deviation of the last digit of the pressure.

Figure 3 shows that an increase in pressure induces a centroid red-shift, broadening, and intensity loss in all four PL bands. The red-shift is due to the stronger crystal field generated by shrinking Tb−O bonds, while the broadening can be attributed to strain, local symmetry distortion, and defect generation.[16,34,47] The intensity loss is likely attributable to pressure-induced increases in electron−phonon coupling, phonon energy, and modified selection rules.[16,39] In the spectra collected after decompression (recov.), the red-shift is largely reversible, while the broadening is largely maintained; these effects are exemplified by band 4 in panels a and b of Figure 3. However, some broadening is reversed upon pressure release as revealed by the full width at half-maximum (FHWM) values of band 4 (see Figure SI.3). The partial reversibility of the PL fwhm is likely attributable to residual strain, distortion, and defects as well as metastable monazite remaining in the sample after decompression. The intensity increases upon pressure release; however, the intensity is not systematically analyzed because it varies with optical focus, which is manually adjusted at each pressure step in the experiments. Quantitative band centroid data and additional reversibility analysis are presented below. Across three separate experiments, PL peaks newly emerge or grow at pressures near the XRD-based xenotime−monazite P_{onset} of 8.7(6) GPa (as shown in panels a and b of Figure 3).[31] Such peaks are located in band 1 at ∼500 nm, in band 2 at ∼535 and ∼555 nm, and in

https://doi.org/10.1021/acs.jpclett.4c00196
J. Phys. Chem. Lett. 2024, 15, 4294−4300

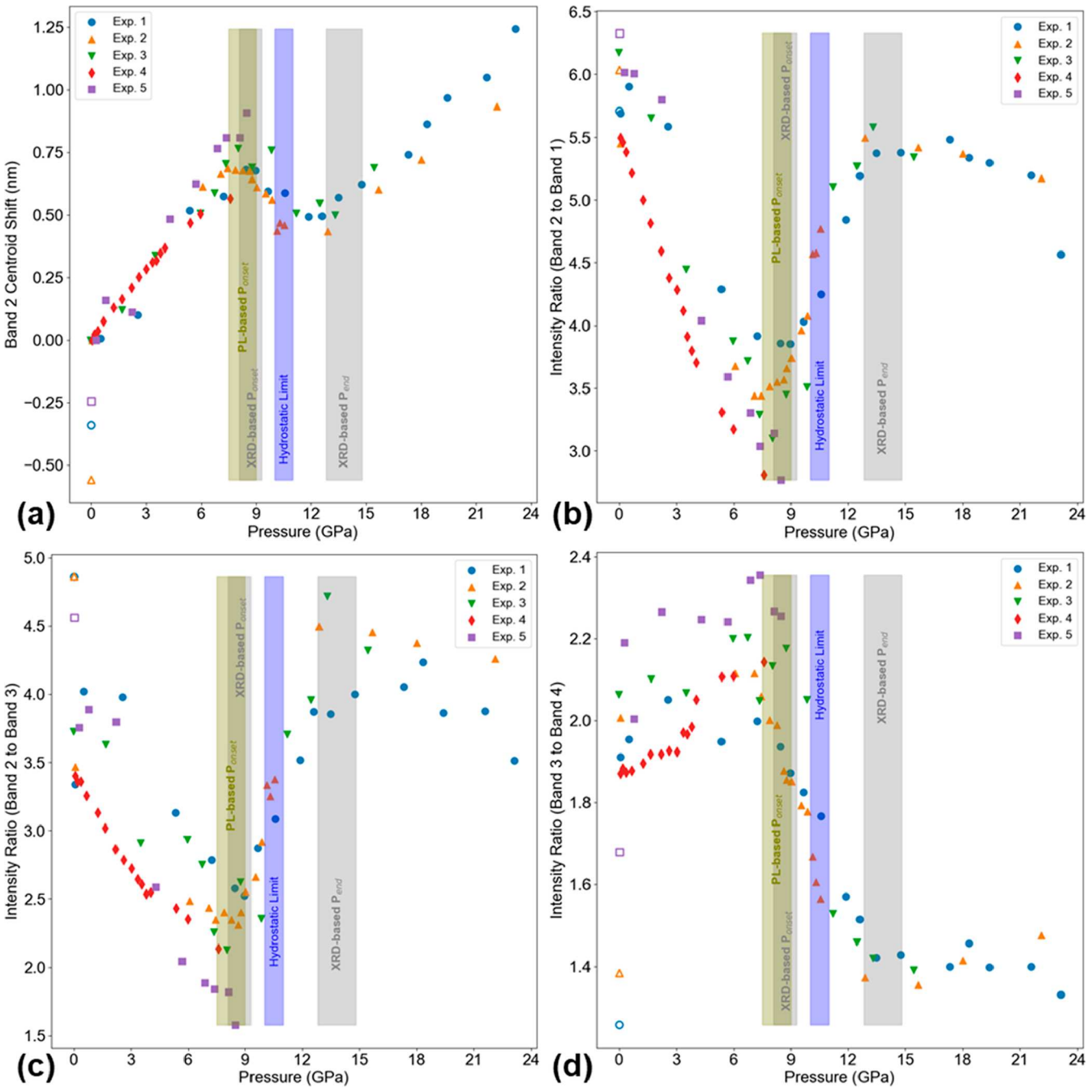

Figure 4. Pressure evolution of selected $TbPO_4$ PL band metrics compiled from all experiments. Olive, blue, and gray rectangles represent pressure ranges corresponding to the PL-based onset of structural distortion, the hydrostatic limit of MEW, and the xenotime−monazite phase coexistence range (as reported by Lopez-Solano et al.),[32] respectively. Empty symbols represent data from the recovered sample at 1 atm. Pressure error bars are within the symbols. (a) Band 2 centroid shift (with respect to its initial value in each experiment). (b) Ratio of the intensity of band 2 to that of band 1. (c) Ratio of the intensity of band 2 to that of band 3. (d) Ratio of the intensity of band 3 to that of band 4.

band 3 at ∼580 and ∼590 nm. The presence of additional peaks suggests the local environment loses symmetry, which is consistent with the Tb^{3+} point group change ($D_{2d} \rightarrow C_1$) during the xenotime−monazite transformation. The evolution of the overall shape of band 2 above 10 GPa is also consistent with the PL spectrum of monazite $TbPO_4$ reported by Yang et al.[41] The shapes of bands 1, 3, and 4 are not compared to those in Yang et al. because these bands are not markedly different between the xenotime and monazite phases.

Nevertheless, the emergence and growth of PL peaks at pressures consistent with an XRD-based xenotime−monazite P_{onset} of 8.7(6) GPa strongly indicate that the PL of Tb^{3+} reveals the xenotime−monazite phase transformation in $TbPO_4$. PL spectra from Exp. 3, as shown in Figure SI.4, also included pressures above P_{onset} and yielded findings consistent with those of Exp. 1 and Exp. 2. PL spectra from Exp. 4 and Exp. 5 (see Figures SI.5 and SI.6) did not exceed P_{onset} but did show the red-shift, broadening, and intensity loss observed in Exp. 1 and Exp. 2 below P_{onset}. Exp. 5 also shows residual broadening in the recovered sample, which is consistent with Exp. 1 and Exp. 2, and indicates residual broadening is not caused exclusively by phase transformation.

https://doi.org/10.1021/acs.jpclett.4c00196
J. Phys. Chem. Lett. 2024, 15, 4294−4300

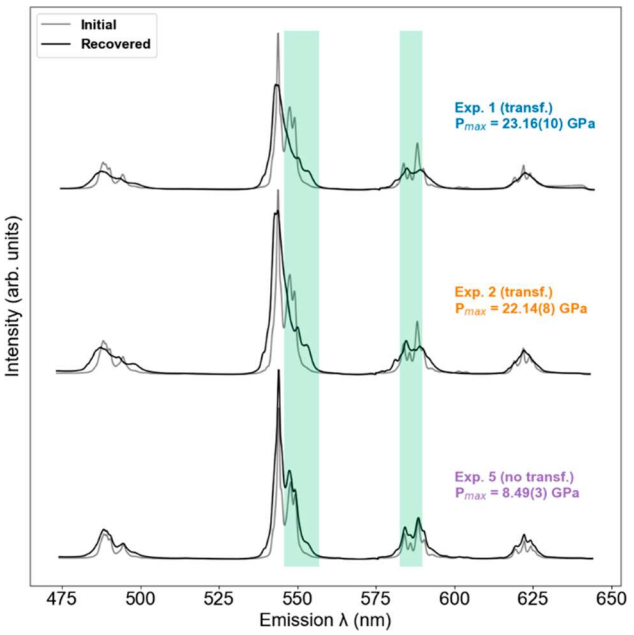

Figure 5. Initial and recovered $TbPO_4$ PL spectra overlaid for comparison from Exp. 1, Exp. 2, and Exp. 5. Sections of the spectra that most clearly indicate a history of phase transformation are highlighted in green.

Figure 4 shows the pressure dependence of selected PL band metrics, which appear to be early indicators of the xenotime−monazite transformation. These band metrics are also placed in context with the hydrostatic limit of MEW [10.5(5) GPa][48] and the XRD-based $TbPO_4$ xenotime−monazite coexistence range during phase transformation [8.7(6)−13.7(10) GPa].[31] The pressure dependencies of other PL band metrics with weaker changes around P_{onset} are included in Figures SI.7 and SI.8.

Figure 4a shows shifts in the band 2 centroid (i.e., change from its initial value at ∼0 GPa). The band 2 centroid red-shifts until ∼8 GPa (as marked by the olive bar), which is statistically significantly lower than the hydrostatic limit and XRD-based P_{onset}. After ∼8 GPa, the band 2 centroid begins to blue-shift and then red-shifts again at ∼13.5 GPa (consistent with the XRD-based P_{end}). The blue-shift may be understood as a weakening of the crystal field due to the Tb−O bond reconfiguration during the xenotime−monazite phase transformation. Figure 4a also shows the band 2 centroid does not return to its initial value in the recovered sample (open data points at ∼1 atm), and this residual centroid shift is noticeably greater in experiments in which phase transformation occurred. The band 3 centroid behaves like the band 2 centroid in the aforementioned ways and is shown in Figure SI.7b. Band centroid hysteresis suggests some irreversible pressure-induced changes (i.e., material stress history) can be detected using PL band metrics.

Panels b−d of Figure 4 show the pressure dependence of selected BIRs. Similar to the band 2 centroid, these BIRs exhibit clear trend changes prior to P_{onset} and at P_{end}. Figure 4b shows the 2:1 BIR decreases until ∼8 GPa, starts increasing steeply, and then appears to stabilize or slightly decrease at P_{end}. Figure 4c shows nearly identical behavior at the 2:3 BIR. Figure 4d shows that the 3:4 BIR undergoes less dramatic trend changes in the opposite directions of the trend changes in the previous BIRs. The first 3:4 BIR trend change also occurs at a slightly lower pressure of ∼7.5 GPa. Across all three BIRs, the pressure range in which the first trend change occurs (i.e., the inferred PL-based onset of distortion shown as an olive rectangle) is always statistically significantly lower than the hydrostatic limit and coincides with XRD-based P_{onset}. Figure 4 also shows that the inferred PL-based onset of distortion varies between band metrics. Such variation between band metrics is also observed during the xenotime−monazite transformation of YPO_4:Yb^{3+},Tm^{3+} and is likely caused by variation in the symmetry sensitivity of the emissions involved.[16,39] When considering the data points from the recovered samples, the 2:3 BIR (Figure 4c) appears to have a larger residual hysteresis than the 2:1 and 3:4 BIRs (Figure 4b,d). In addition, the 3:1 BIR shown in Figure SI.8a exhibits a residual hysteresis in the recovered sample, and this hysteresis is greater in experiments in which phase transformation occurred. Overall, the magnitude of the pressure-induced changes of the 2:1, 2:3, and 3:4 BIRs and the magnitude of their hystereses make them better potential indicators of stress history than band centroids.

Figure 5 overlays initial and recovered $TbPO_4$ PL spectra from Exp. 1, Exp. 2, and Exp. 5, showing pressure-induced PL changes are more reversible in the absence of phase transformation (Exp. 5). When phase transformation does not occur (Exp. 5), residual broadening is still present in the recovered spectrum, indicating pressure-induced strain/distortion and defect generation are not fully reversible. When phase transformation occurs (Exp. 1 and Exp. 2), the recovered spectra show residual broadening as well as additional peaks (peaks that appeared only after P_{onset}). The clearest indicators of the phase transformation history in Figure 5 are the sections of bands 2 and 3 highlighted in green. While insight into strain and phase memory can be deduced from synchrotron XRD or RS, PL contains complementary information about the material phase and unique electronic and chemical information, including the RE^{3+} coordination environment, RE^{3+}−RE^{3+} energy transfer pathways, local bonding, and redox state. In addition, PL contains information about any potential heterogeneity in these properties via spectral broadening and lifetime that may occur due to hysteretic effects throughout phase transformations. Moreover, circularly polarized PL could offer magnetic information for other RE^{3+} ions with unpaired spins.

In conclusion, this study demonstrates that the pressure-induced xenotime−monazite phase transformation of $TbPO_4$ can be probed using direct excitation PL spectroscopy. Under UV excitation, the intrinsic Tb^{3+} ions generate four PL emission bands in the visible range, and these bands shift and broaden with pressure. Qualitative analysis of the PL spectra shows additional peaks emerging at HP, which is consistent with the Tb^{3+} site symmetry loss during transformation. Quantitative analysis shows the band 2 centroid and the 2:1, 2:3, and 3:4 BIRs undergo clear trend changes at pressures coinciding with XRD-based P_{onset} and P_{end}. The close agreement between the inferred PL-based P_{onset} and the XRD-based P_{onset} shows changes in the RE^{3+} crystal field, as observed via PL spectroscopy, can be used to detect the xenotime−monazite transformation. In addition, PL spectra of the recovered samples indicate metastable monazite exists after decompression, confirming the irreversibility of the xenotime−monazite phase transformation. Hysteresis in certain PL band metrics also serves as a potential gauge of the stress history of the sample. Given the ease of RE substitution in $REPO_4$s and

https://doi.org/10.1021/acs.jpclett.4c00196
J. Phys. Chem. Lett. 2024, 15, 4294−4300

other materials, the analysis of RE^{3+} PL in this work can potentially be extended beyond $TbPO_4$ to other RE-containing oxide compounds (e.g., $REXO_4$s where X = V, As, W, Nb, or Mo).

■ ASSOCIATED CONTENT

Data Availability Statement

All relevant data that support the findings of this study are available from the corresponding authors upon request.

Supporting Information

The Supporting Information is available free of charge at https://pubs.acs.org/doi/10.1021/acs.jpclett.4c00196.

> Additional details about sample synthesis, phase purity, powder morphology, PL measurement, a table showing experimental specific details, and additional figures showing band 4 fwhm data, stacked PL spectra from Exp. 3−Exp. 5, pressure evolution of other centroids (bands 1, 3, and 4) and other BIRs (3:1, 1:4, and 2:4), and loading rates from all experiments (PDF)

■ AUTHOR INFORMATION

Corresponding Author

Corinne E. Packard − *Department of Metallurgical and Materials Engineering, Colorado School of Mines, Golden, Colorado 80401, United States;* orcid.org/0000-0002-5815-8586; Email: cpackard@mines.edu

Authors

Jai Sharma − *Department of Metallurgical and Materials Engineering, Colorado School of Mines, Golden, Colorado 80401, United States;* orcid.org/0000-0003-3903-4534

Brandon Reynolds − *Department of Chemical and Biological Engineering, Colorado School of Mines, Golden, Colorado 80401, United States*

Matthew J. Crane − *Department of Chemical and Biological Engineering, Colorado School of Mines, Golden, Colorado 80401, United States;* orcid.org/0000-0001-8461-4808

Complete contact information is available at: https://pubs.acs.org/10.1021/acs.jpclett.4c00196

Author Contributions

Conceptualization: J.S. Data curation: J.S. and B.R. Formal analysis: J.S. and B.R. Writing of the original draft: J.S. and B.R. Review and editing: J.S., B.R., M.J.C., and C.E.P. Supervision: M.J.C. and C.E.P. Funding acquisition: M.J.C. and C.E.P. All authors have given approval to the final version of the manuscript.

Notes

The authors declare no competing financial interest.

■ ACKNOWLEDGMENTS

The authors thank Dr. Ivar Reimanis for lending his Diacell Helios DAC. This research was supported by the National Science Foundation under Grants DMR-1352499 (C.E.P.) and CMMI-2240479 (M.J.C. and B.R.) and by start-up funds from the Colorado School of Mines. J.S. was supported by the Department of Defense through the National Defense Science & Engineering Graduate Fellowship Program.

■ REFERENCES

(1) Boatner, L. A. Synthesis, Structure, and Properties of Monazite, Pretulite, and Xenotime. *Rev. Mineral. Geochemistry* **2002**, *48* (1), 87−121.

(2) Cox, M. A.; Cavosie, A. J.; Poelchau, M.; Kenkmann, T.; Bland, P. A.; Miljković, K. Shock Deformation Microstructures in Xenotime from the Spider Impact Structure, Western Australia. In *Large Meteorite Impacts and Planetary Evolution VI*; Geological Society of America, 2021; pp 449−464.

(3) Vielreicher, N. M.; Groves, D. I.; Fletcher, I. R.; McNaughton, N. J.; Rasmussen, B. Hydrothermal Monazite and Xenotime Geochronology: A New Direction for Precise Dating of Orogenic Gold Mineralization. *SEG Discovery* **2003**, *70* (53), 1−16.

(4) Erickson, T. M.; Timms, N. E.; Pearce, M. A.; Cayron, C.; Deutsch, A.; Keller, L. P.; Kring, D. A. Shock-Produced High-Pressure (La, Ce, Th)PO_4 Polymorph Revealed by Microstructural Phase Heritage of Monazite. *Geology* **2019**, *47* (6), 504−508.

(5) Van Hoozen, C. J.; Gysi, A. P.; Harlov, D. E. The Solubility of Monazite ($LaPO_4$, $PrPO_4$, $NdPO_4$, and $EuPO_4$) Endmembers in Aqueous Solutions from 100 to 250 °C. *Geochim. Cosmochim. Acta* **2020**, *280*, 302−316.

(6) Liu, J.; Han, W.; Chen, X.; Zhong, D.; Teng, B.; Wang, C.; Li, Y. Spectroscopic Properties and Continuous-Wave Laser Operation of Yb:$LuPO_4$ Crystal. *Opt. Lett.* **2014**, *39* (20), 5881.

(7) Zeler, J.; Zych, E.; Jedoń, J. $LuPO_4$:Yb Phosphor with Concerted UV and IR Thermoluminescent Emissions by Quantum Cutting at High Temperatures. *Phys. Chem. Chem. Phys.* **2019**, *21* (43), 23826−23832.

(8) Steudel, F.; Loos, S.; Ahrens, B.; Schweizer, S. Quantum Efficiency and Energy Transfer Processes in Rare-Earth Doped Borate Glass for Solid-State Lighting. *J. Lumin.* **2016**, *170*, 770−777.

(9) Wojtowicz, A. J.; Wenewski, D.; Lempicki, A.; Boatner, L. A. Scintillation Mechanisms in Rare Earth Orthophosphates. *Radiat. Eff. Defects Solids* **1995**, *135* (1−4), 305−310.

(10) Boatner, L. A.; Keefer, L. A.; Farmer, J. M.; Wisniewski, D.; Wojtowicz, A. J. Cerium-Activated Rare-Earth Orthophosphate and Double-Phosphate Scintillators for X- and Gamma-Ray Detection. *SPIE Proc.* **2004**, *5540*, 73.

(11) Morgan, P. E. D.; Marshall, D. B. Functional Interfaces for Oxide/Oxide Composites. *Mater. Sci. Eng., A* **1993**, *162* (1−2), 15−25.

(12) Morgan, P. E. D.; Marshall, D. B. Ceramic Composites of Monazite and Alumina. *J. Am. Ceram. Soc.* **1995**, *78* (6), 1553−1563.

(13) Hay, R. S.; Mogilevsky, P.; Boakye, E. Phase Transformations in Xenotime Rare-Earth Orthophosphates. *Acta Mater.* **2013**, *61* (18), 6933−6947.

(14) Hay, R. S.; Boakye, E. E.; Mogilevsky, P.; Fair, G. E.; Parthasarathy, T. A.; Davis, J. E. Transformation Plasticity in $(Gd_xDy_{1-x})PO_4$ Fiber Coatings During Fiber Push Out. *J. Am. Ceram. Soc.* **2013**, *96* (5), 1586−1595.

(15) Gangwar, P.; Pandey, M.; Sivakumar, S.; Pala, R. G. S.; Parthasarathy, G. Increased Loading of Eu^{3+} Ions in Monazite LaVO4 Nanocrystals via Pressure-Driven Phase Transitions. *Cryst. Growth Des.* **2013**, *13* (6), 2344−2349.

(16) Runowski, M.; Shyichuk, A.; Tymiński, A.; Grzyb, T.; Lavín, V.; Lis, S. Multifunctional Optical Sensors for Nanomanometry and Nanothermometry: High-Pressure and High-Temperature Upconversion Luminescence of Lanthanide-Doped Phosphates—$LaPO_4$/YPO_4:Yb^{3+} − Tm^{3+}. *ACS Appl. Mater. Interfaces* **2018**, *10* (20), 17269−17279.

(17) Sheik-Bahae, M.; Epstein, R. I. Laser Cooling of Solids. *Laser Photon. Rev.* **2009**, *3* (1−2), 67−84.

(18) Miyazono, E.; Zhong, T.; Craiciu, I.; Kindem, J. M.; Faraon, A. Coupling of Erbium Dopants to Yttrium Orthosilicate Photonic Crystal Cavities for On-Chip Optical Quantum Memories. *Appl. Phys. Lett.* **2016**, *108* (1), 11111.

(19) Kindem, J. M.; Bartholomew, J. G.; Woodburn, P. J. T.; Zhong, T.; Craiciu, I.; Cone, R. L.; Thiel, C. W.; Faraon, A. Characterization

of Yb^{3+}:YVO_4 for Photonic Quantum Technologies. *Phys. Rev. B* **2018**, *98* (2), No. 024404.
(20) Kumar, V.; Singh, S.; Chawla, S. Fabrication of Dual Excitation, Dual Emission Nanophosphor with Broad UV and IR Excitation through Simultaneous Doping of Triple Rare Earth Ions Er^{3+}, Yb^{3+}, Eu^{3+} in $GdPO_4$. *Superlattices Microstruct.* **2015**, *79*, 86−95.
(21) Vergeer, P.; Vlugt, T. J. H.; Kox, M. H. F.; Den Hertog, M. I.; van der Eerden, J. P. J. M.; Meijerink, A. Quantum Cutting by Cooperative Energy Transfer in $Yb_xY_{1-x}PO_4$:Tb^{3+}. *Phys. Rev. B* **2005**, *71* (1), 014119.
(22) Ni, Y.; Hughes, J. M.; Mariano, A. N. Crystal Chemistry of the Monazite and Xenotime Structures. *Am. Mineral.* **1995**, *80* (1−2), 21−26.
(23) Sharma, J.; Musselman, M.; Haberl, B.; Packard, C. E. In Situ Synchrotron Diffraction of Pressure-Induced Phase Transition in $DyPO_4$ under Variable Hydrostaticity. *Phys. Rev. B* **2021**, *103* (18), No. 184105.
(24) Musselman, M. A.; Wilkinson, T. M.; Haberl, B.; Packard, C. E. In Situ Raman Spectroscopy of Pressure-Induced Phase Transformations in Polycrystalline $TbPO_4$, $DyPO_4$, and $Gd_xDy_{(1-x)}PO_4$. *J. Am. Ceram. Soc.* **2018**, *101* (6), 2562−2570.
(25) Sharma, J.; Afful, H. Q.; Packard, C. E. Phase Transformation Pathway of $DyPO_4$ to 21.5 GPa. *Cryst. 2023, Vol. 13, Page 249* **2023**, *13* (2), 249.
(26) Li, H.; Zhang, S.; Zhou, S.; Cao, X. Bonding Characteristics, Thermal Expansibility, and Compressibility of RXO_4 (R = Rare Earths, X = P, As) within Monazite and Zircon Structures. *Inorg. Chem.* **2009**, *48* (10), 4542−4548.
(27) Heuser, J. M.; Neumeier, S.; Peters, L.; Schlenz, H.; Bosbach, D.; Deissmann, G. Structural Characterisation of Metastable Tb- and Dy-Monazites. *J. Solid State Chem.* **2019**, *273*, 45−52.
(28) Momma, K.; Izumi, F. VESTA 3 for Three-Dimensional Visualization of Crystal, Volumetric and Morphology Data. *J. Appl. Crystallogr.* **2011**, *44* (6), 1272−1276.
(29) Tatsi, A.; Stavrou, E.; Boulmetis, Y. C.; Kontos, A. G.; Raptis, Y. S.; Raptis, C. Raman Study of Tetragonal $TbPO_4$ and Observation of a First-Order Phase Transition at High Pressure. *J. Phys.: Condens. Matter* **2008**, *20* (42), 425216.
(30) Musselman, M. A. In Situ Raman Spectroscopy of Pressure-Induced Phase Transformations in $DyPO_4$ and $Gd_xDy_{(1-x)}PO_4$. Ph.D. Dissertation, Colorado School of Mines, Golden, CO, 2017.
(31) Sharma, J.; Packard, C. E. Uncovering the Effects of Non-Hydrostaticity on Pressure-Induced Phase Transformation in Xenotime-Structured $TbPO_4$. *Solids* **2024**, *5* (1), 110−122.
(32) López-Solano, J.; Rodríguez-Hernández, P.; Muñoz, A.; Gomis, O.; Santamaría-Perez, D.; Errandonea, D.; Manjón, F. J.; Kumar, R. S.; Stavrou, E.; Raptis, C. Theoretical and Experimental Study of the Structural Stability of $TbPO_4$ at High Pressures. *Phys. Rev. B - Condens. Matter Mater. Phys.* **2010**, *81* (14), 1−9.
(33) Zhang, C. C.; Zhang, Z. M.; Dai, R. C.; Wang, Z. P.; Zhang, J. W.; Ding, Z. J. High-Pressure Raman and Luminescence Study on the Phase Transition of $GdVO_4$:Eu^{3+} Microcrystals. *J. Phys. Chem. C* **2010**, *114* (42), 18279−18282.
(34) Zhao, Z.; Zuo, J.; Ding, Z. Pressure Effect on Optical Properties and Structure Stability of $LaPO_4$:Eu^{3+} Hollow Spheres. *J. Rare Earths* **2010**, *28*, 254−257.
(35) Lenz, C.; Nasdala, L.; Talla, D.; Hauzenberger, C.; Seitz, R.; Kolitsch, U. Laser-Induced REE^{3+} Photoluminescence of Selected Accessory Minerals - An "Advantageous Artefact" in Raman Spectroscopy. *Chem. Geol.* **2015**, *415*, 1−16.
(36) Sharma, S. K.; Behm, T.; Köhler, T.; Beyer, J.; Gloaguen, R.; Heitmann, J. Library of UV-Visible Absorption Spectra of Rare Earth Orthophosphates, $LnPO^4$ (Ln = La-Lu, except Pm). *Crystals* **2020**, *10* (7), 593.
(37) Fuchs, M. C.; Beyer, J.; Lorenz, S.; Sharma, S.; Renno, A. D.; Heitmann, J.; Gloaguen, R. A Spectral Library for Laser-Induced Fluorescence Analysis as a Tool for Rare Earth Element Identification. *Earth Syst. Sci. Data* **2021**, *13* (9), 4465−4483.
(38) Roh, J. Y. D.; Smith, M. D.; Crane, M. J.; Biner, D.; Milstein, T. J.; Krämer, K. W.; Gamelin, D. R. Yb^{3+} Speciation and Energy-Transfer Dynamics in Quantum-Cutting Yb^{3+} -Doped $CsPbCl_3$ Perovskite Nanocrystals and Single Crystals. *Phys. Rev. Mater.* **2020**, *4* (10), 1−11.
(39) Runowski, M. Pressure and Temperature Optical Sensors: Luminescence of Lanthanide-Doped Nanomaterials for Contactless Nanomanometry and Nanothermometry. In *Handbook of Nanomaterials in Analytical Chemistry*; Elsevier, 2020; pp 227−273.
(40) Lösch, H.; Hirsch, A.; Holthausen, J.; Peters, L.; Xiao, B.; Neumeier, S.; Schmidt, M.; Huittinen, N. A Spectroscopic Investigation of Eu^{3+} Incorporation in $LnPO_4$ (Ln = Tb, $Gd_{1-X}Lu_X$, X = 0.3, 0.5, 0.7, 1) Ceramics. *Front. Chem.* **2019**, *7* (FEB), 94.
(41) Yang, M.; You, H.; Song, Y.; Huang, Y.; Jia, G.; Liu, K.; Zheng, Y.; Zhang, L.; Zhang, H. Synthesis and Luminescence Properties of Sheaflike $TbPO_4$ Hierarchical Architectures with Different Phase Structures. *J. Phys. Chem. C* **2009**, *113* (47), 20173−20177.
(42) Khan, D. T.; Dang, N. T.; Jabarov, S. H.; Naghiyev, T. G.; Rzayev, R. M.; Nguyen, T. Q.; Tuyen, H. V.; Thanh, N. T.; Son, L. V. T. Study on Luminescent Properties of Tb^{3+} and Sm^{3+} Co-Doped $CaSiO_3$ Phosphors for White Light Emitting Diodes. *Mater. Res. Express* **2020**, *7* (1), No. 016507.
(43) Lösch, H.; Hirsch, A.; Holthausen, J.; Peters, L.; Neumeier, S.; Huittinen, N. Site-Selective Fluorescence Spectroscopy Investigations of $LnPO_4$ Xenotime Ceramics for Radioactive Waste Disposal. Institute of Resource Ecology, 2016; Vol. *13*.
(44) Dieke, G. H.; Crosswhite, H. M.; Dunn, B. Emission Spectra of the Doubly and Triply Ionized Rare Earths*. *J. Opt. Soc. Am.* **1961**, *51* (8), 820.
(45) Qin, X.; Liu, X.; Huang, W.; Bettinelli, M.; Liu, X. Lanthanide-Activated Phosphors Based on 4f-5d Optical Transitions: Theoretical and Experimental Aspects. *Chem. Rev.* **2017**, *117* (5), 4488−4527.
(46) Shen, G.; Wang, Y.; Dewaele, A.; Wu, C.; Fratanduono, D. E.; Eggert, J.; Klotz, S.; Dziubek, K. F.; Loubeyre, P.; Fat'yanov, O. V.; Asimow, P. D.; Mashimo, T.; Wentzcovitch, R. M. M. Toward an International Practical Pressure Scale: A Proposal for an IPPS Ruby Gauge (IPPS-Ruby2020). *High Press. Res.* **2020**, *40* (July), 299−314.
(47) Goderski, S.; Runowski, M.; Woźny, P.; Lavín, V.; Lis, S. Lanthanide Upconverted Luminescence for Simultaneous Contactless Optical Thermometry and Manometry-Sensing under Extreme Conditions of Pressure and Temperature. *ACS Appl. Mater. Interfaces* **2020**, *12* (36), 40475−40485.
(48) Klotz, S.; Chervin, J.-C.; Munsch, P.; Le Marchand, G. Hydrostatic Limits of 11 Pressure Transmitting Media. *J. Phys. D. Appl. Phys.* **2009**, *42* (7), No. 075413.

https://doi.org/10.1021/acs.jpclett.4c00196
J. Phys. Chem. Lett. 2024, 15, 4294−4300